10-2011

Region-of-Interest Material Decomposition From Truncated Energy-Resolved CT

Taly Gilat Schmidt
Marquette University, tal.gilat-schmidt@marquette.edu

Medical Physics, Vol. 38, No. 10 (October 2011): 5657-5666. DOI.

Region-Of-Interest Material Decomposition from Truncated Energy-Resolved CT

Taly Gilat Schmidt
Department of Biomedical Engineering, Marquette University, Milwaukee, Wisconsin
Fatih Pektas
Department of Biomedical Engineering, Marquette University, Milwaukee, Wisconsin

Abstract

Purpose:

Energy-resolved CT using photon-counting detectors has the potential to provide improved material decomposition compared to dual-kVp approaches. However, available photon-counting detectors are susceptible to pulse-pileup artifacts, especially at the periphery of the field of view (FOV) where the object attenuation is low compared to the center of the FOV. Pulse pileup may be avoided by imaging a region-of-

interest (ROI) where the dynamic range is expected to be limited. This work investigated performing material decomposition and reconstructing ROI basis images from truncated energy-resolved data.

Methods:

A method is proposed to reconstruct images of basis functions primarily contained within the ROI, such as targeted or localized K-edge contrast agents. Material decomposition is performed independently for each ray in the sinogram, followed by filtered backprojection from the truncated data encompassing the ROI. A second method is proposed that uses a prior conventional energy-integrating image to estimate energy-resolved data outside the ROI. The measured and estimated energy-resolved data are decomposed into basis projections and merged into basis sinograms of the full FOV. Basis images of the ROI are then reconstructed through filtered backprojection. This method is most easily applied to objects that do not contain K-edge contrast agents outside the ROI. Simulations of a voxelized thorax phantom with iodine in the blood pool and a detector with five energy bins were performed. Full FOV, truncated, and truncated data merged with data estimated from the prior energy-integrating image were decomposed into Compton, photoelectric, and iodine basis functions. An empirical weighting factor was determined to blend the merged sinogram at the boundary of the truncated data. The effects of noise and misalignment in the prior image were also quantified. Basis images of the central 15 cm × 15 cm ROI containing the heart were reconstructed via filtered backprojection. Basis image accuracy was quantified relative to gold-standard basis images reconstructed from full FOV energy-resolved data.

Results:

The error in the iodine basis image reconstructed from truncated energy-resolved data without prior information was less than 1% for the central 7 cm of the 7.5-cm-radius ROI and 3% at the edge of the ROI. When the truncated and estimated basis sinograms were blended, the error was below 1% throughout the ROI for photoelectric basis images and ranged from 1% at the center of the ROI to 4% at the edge for the Compton basis image.

Conclusions:

The density of localized K-edge contrast agents can be estimated to within 1% error using filtered back projection without prior information. For noncontrast and localized-contrast scans, ROI images of general basis functions can be reconstructed to within a few percent error using a prior energy-integrating image. The ability to perform material decomposition for a limited ROI may facilitate energy-resolved CT with available photon-counting detectors.

I. INTRODUCTION

Material decomposition in CT imaging has shown promise in numerous applications including the improved depiction of the vessel lumen, single-phase contrast scans, kidney stone characterization, and quantification of fat and iron content in the liver.[1–6] Material decomposition is possible when projections are acquired at multiple energies, for example, by performing high and low kVp acquisitions.[7] Energy-resolving detectors, fabricated from direct-conversion semiconductors such as CdZnTe or CdTe, perform pulse-height analysis with a series of comparators to sort detected photons into discrete energy-bins.[8] Potential advantages of energy-resolved CT compared to dual-kVp methods include the ability to decompose an object into more than two materials, reduced spectral overlap, and simultaneous acquisition of multienergy data.[9–12] Energy-resolved CT recently demonstrated feasibility of imaging targeted molecular K-edge contrast agents, for example, to characterize plaque composition.[13,14]

One challenge of photon-counting energy-resolved detection is the potential for pulse-pileup effects caused by limited count rates.[15] For example, typical CT acquisitions require detected count rates as high as

10^9 photons/(mm^2 s), while state-of-the art photon-counting detectors provide rates of 10^7 photons/(mm^2 s).[12,16] Bowtie filtration reduces the detected flux toward the periphery of elliptical and cylindrical objects; however, ideal bowtie filtration is difficult to achieve in practice. Therefore, available photon-counting detector technology may be susceptible to pulse-pileup artifacts, especially toward the periphery of the field of view (FOV).[17] Several methods for improving the count rate of photon-counting detectors are being investigated, for example, smaller pixels and layered pixels.[17,18] Methods were also proposed for correcting pulse-pileup effects.[16,19,20]

A previous study proposed reducing pulse-pileup effects by acquiring truncated photon-counting projection data of a region-of-interest (ROI) for which the dynamic range is expected to be limited.[21] A requirement of conventional CT reconstruction is that the entire object must be imaged even if only a limited region will be reconstructed. Advanced reconstruction algorithms were proposed to relax this constraint; however, the algorithms are not applicable to all truncation cases.[22–25] Theoretically, exact reconstruction of an interior ROI from truncated projection data is possible with prior knowledge of a small region in the ROI.[25] The algorithm may become unstable for points in the ROI sampled by less than 180° of views. The previous study of ROI photon-counting CT used this tiny *a priori* algorithm to reconstruct conventional CT images (i.e., without material decomposition).[21] A modification of the tiny *a priori* algorithm was proposed that assumes knowledge that a small region of the image is piecewise constant.[26] The modified algorithm uses a combination of filtered backprojection, total variation minimization, and differentiation-backprojection onto convex sets to reconstruct images.

While advanced reconstruction algorithms are one approach to ROI imaging, hardware solutions were also proposed for acquiring conventional CT data within an ROI and reduced quality data outside the ROI.[27–31] For example, one study used a high-resolution detector within the ROI and a lower resolution detector for the remaining FOV.[27] A different approach increased filtration to reduce dose outside the ROI.[27,30] Commercial dual-source CT systems use one detector, that is, smaller than the FOV. Data from the smaller detector are extrapolated using the full FOV projections, and material decomposition is performed after image reconstruction.[32] These ROI CT systems demonstrated that data reconstructed within the ROI were not degraded by the increased noise or decreased resolution outside the ROI, due to the relatively local nature of the convolution kernels used for filtered backprojection.

This study proposes acquiring truncated energy-resolved CT data, performing material decomposition in sinogram space, and reconstructing basis images for an ROI. We investigate one method for cases in which one or more basis images are contained within the ROI, as may be possible with K-edge contrast agents. Because material decomposition is performed in sinogram space, the basis image with limited FOV can be reconstructed from the truncated data without prior information. The second proposed method applies to material decomposition for a general set of basis functions. The method acquires truncated energy-resolved CT data for a limited ROI, while acquiring conventional energy-integrating data for the full FOV. The energy-integrating data are used as prior information for reconstructing basis images within the ROI. The prior energy-integrating method is most easily applied to noncontrast scans and objects with K-edge contrast agents localized within the ROI.

The two proposed methods of ROI material decomposition from truncated energy-resolved data were studied through simulations of a voxelized thorax phantom. The accuracy of the resulting basis images was quantified relative to images obtained from full FOV energy-resolved CT.

II. METHODS AND MATERIALS

II.A. Material decomposition

The attenuation coefficient of any material can be decomposed into two basis functions if x-ray projections are acquired at two or more energies. This is possible because two distinct energy-dependent processes primarily determine x-ray attenuation in the diagnostic imaging range: Compton scatter and photoelectric absorption.[7] Common basis functions are the photoelectric and Compton attenuation functions or the attenuation coefficient functions of two basis materials. The decomposed attenuation coefficient is represented by Eq. (1)[7,33]

$$\mu(E) = c_1\mu_1(E) + c_2\mu_2(E),$$

(1)

where μ_1 and μ_2 are the basis functions and c_1 and c_2 are the coefficients representing the contribution of each basis function. For example, if μ_1 and μ_2 represent the mass attenuation coefficients of two basis materials, c_1 and c_2 represent the local density or concentration (g/cm^3) of each basis material, respectively. Previous work showed that an object can be decomposed into more than two materials, if the additional basis functions are equal to the attenuation coefficient of materials with K-edges in the acquired energy range and projections are acquired at a number of energies equal to or greater than the number of basis functions.[11,12] The decomposition into two basis functions described in Eq. (1) can be expanded to multiple basis functions as expressed in Eq. (2)

$$\mu(E) = \sum_{i=1}^{M} c_i\mu_i(E),$$

(2)

where M is the number basis functions.

The unknown basis coefficients, c_i, are estimated by acquiring projection data at multiple energies and solving the resulting nonlinear system of equations. The number of photons detected in B energy bins for a ray t can be expressed as

$$\begin{aligned} N_1 &= \int_{E_1} N_o(E)\exp\left[-\sum c_i \int \mu_i(E,t)dt\right]dE, \\ N_2 &= \int_{E_2} N_o(E)\exp\left[-\sum c_i \int \mu_i(E,t)dt\right]dE, \\ &\vdots \\ N_B &= \int_{E_B} N_o(E)\exp\left[-\sum c_i \int \mu_i(E,t)dt\right]dE, \end{aligned}$$

(3)

where E_j is the energy range of the *j*th bin and $N_o(E)$ is the number of photons exiting the source at energy E. If projections are acquired at more energy levels than the number of basis functions, the system of equations is overdetermined and coefficients c_i can be estimated through least-squares or statistical approaches.[7,12,33] For

example, previous work successfully decomposed energy-resolved CT data into Compton, photoelectric, iodine, and gadolinium basis functions.[11,12] Once the projection data at each view angle are decomposed into the basis projections, basis images are reconstructed with conventional CT reconstruction algorithms.

II.B. ROI basis decomposition and reconstruction

Basis images can be reconstructed exactly from truncated data, if the contribution of the corresponding basis function is zero outside of the truncated data. This is possible if material decomposition is performed independently for each ray in the sinogram. Specifically, energy-resolved data are collected in *B* energy bins for all rays passing through the ROI containing the localized basis function. For each acquired ray, the projection data from the *B* energy bins are decomposed into *M* basis sinograms. Basis images are then reconstructed from the decomposed truncated sinograms using conventional methods, such as filtered backprojection. This method would be appropriate for studies that require only information about the basis component of limited extent, for example, studies quantifying the concentration of a localized material with a specific K-edge.

For the more general case of arbitrary basis functions, we propose an algorithm for performing material decomposition and reconstructing basis images for a limited ROI using prior energy-integrating data from the entire FOV. The steps of the proposed algorithm are illustrated in Fig. **1**. Energy-integrating detectors image the full FOV, while energy-resolving detectors with *B* energy-bins image a smaller ROI. Images of the full FOV are first reconstructed from the energy-integrating data using a conventional reconstruction technique. The resulting prior image is segmented based on Hounsfield unit (HU) values into *K* materials. A polyenergetic forward projection is performed on the segmented volume to estimate data in the *B* energy bins of detectors outside the ROI.

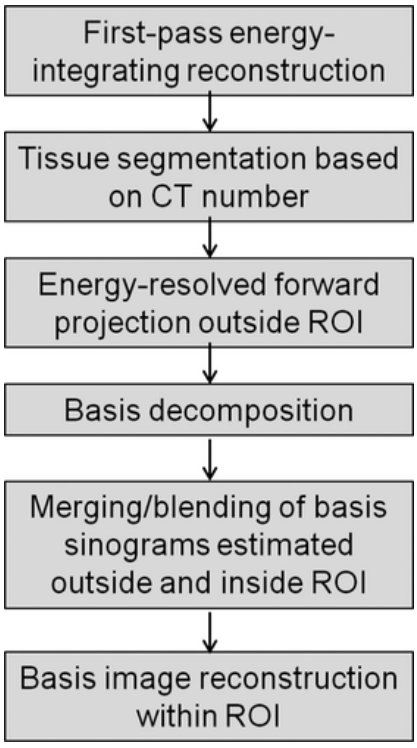

Figure 1. Proposed algorithm for reconstructing ROI basis images from truncated energy-resolved CT data with prior energy-integrating data.

Material decomposition is performed on a ray-by-ray basis for both the measured projection data within the ROI and the estimated energy-resolved data outside the ROI. *M* basis sinograms encompassing the entire FOV are

then formed by merging the basis projections decomposed from the measured and estimated energy-resolved data. Blending the basis sinograms at the boundaries of the truncated data may be performed to reduce discontinuities. Finally, *M* basis images are reconstructed from the decomposed sinograms using conventional techniques (i.e., filtered backprojection).

Because material decomposition is performed independently for each ray, the error in the estimated energy-resolved data outside the ROI does not affect the decomposition into basis sinograms within the ROI. However, the error in the estimated data outside the ROI is expected to introduce errors during ROI basis image reconstruction. For objects with K-edge contrast agents distributed across the FOV, this method requires segmenting the contrast material in the prior energy-integrating image in order to decompose contrast-agent basis functions. Because segmenting the contrast-agent based on HU value may be challenging, the proposed prior-image method is most applicable to noncontrast acquisitions (e.g., kidney stone characterization) and for estimating noncontrast basis functions for objects in which K-edge contrast agents are localized within the ROI (e.g., cardiac imaging and targeted tracers).

II.C. Simulation study

The feasibility of ROI basis image reconstruction with and without prior energy-integrating data was investigated through simulations. The accuracy of the resulting basis images was quantified relative to basis images reconstructed from full FOV energy-resolved CT data.

II.C.1. Phantom

A 2D female thorax phantom was generated from an axial slice of a previously acquired clinical CT dataset that included iodinated contrast material. The CT image, composed of 512 × 512 pixels of size 0.566 mm × 0.566 mm, was segmented by CT number into 22 materials representing eight tissue types, as listed in Table **I**. The HU ranges for segmenting lung, adipose, water, muscle, and bone tissues were proposed by DeMarco *et al*.[34] A region encompassing the lung and heart was manually identified within the CT slice. Pixels in the heart and lung with HU values greater than 280 were segmented into five concentrations of iodine, with iodine weight fractions of 0.013, 0.019, 0.028, 0.036, and 0.049, resulting in the range of densities listed in Table **I**. The iodine weight fractions were chosen empirically to match the HU values in the CT image. The resulting phantom is displayed in Fig. **2**. One bright region in the heart contained pixels with HU > 1500. These pixels were modeled as calcium in order to introduce a task of differentiating iodine from calcium. All simulations assumed attenuation coefficients from the XCOM database and tissue compositions from the ICRU 44 report.[35,36]

Table I. HU ranges used to segment a CT image into a voxelized phantom consisting of 22 materials representing eight tissue types. The densities of the segmented materials are also listed. Voxels in the heart and lung with HU values greater than 280 and 1500 HU were modeled as diluted iodine and calcium, respectively, while voxels outside the heart and lung with HU > 280 were modeled as bone.

	Air	**Lung**	**Adipose**	**Water**	**Muscle**	**Bone**	**Iodine**	**Calcium**
Number of materials	1	6	2	1	2	6	5	1
HU range	−2000 ⇔ −930	−930 ⇔ −200	−200 ⇔ −5	−5 ⇔ 5	5 ⇔ 280	280 ⇔ 1500	280 ⇔ 1500	>1500
Density (g/cm^3)	1.205×10^{-3}	0.1 ⇔ 0.6	0.88, 0.98	1.00	1.11, 1.21	1.53 ⇔ 2.05	1.011 ⇔ 1.041	2

Figure 2. 2D voxelized phantom of a female thorax segmented into 22 materials as described in Table **I**.

II.C.2. Simulation specifications

Table **II** summarizes the specifications of the simulated CT system. The 120 kVp spectrum with 6 mm Al filtration was generated using the SPEC78 software from the IPEM 78 report.[37] The SPEC78 software also estimated ~1E6 photons in the raw beam reaching the central detector pixel for a 200 mAs acquisition. This number of raw-beam photons was simulated for all detector pixels. The energy-resolved detector was simulated with five energy bins assuming ideal energy resolution and unlimited count rate. The energy-bin ranges (Table **II**) were selected heuristically and were not optimized. The boundary between the two lowest energy bins was set at the K-edge of Iodine.

Table II. Simulated system specifications.

Number of detector pixels	700
Pixel size	1 mm
Source-to-isocenter distance	50 cm
Source-to-detector distance	100 cm
Number of views	500
Spectrum	120 kVp, 6 mm Al
mAs	200
Energy-bin ranges	(20–33), (34–41), (42–64), (65–95), (96–120) keV

A polyenergetic ray-tracing algorithm based on the Siddon method was performed to simulate both energy-resolved and energy-integrating data for the 700 detector pixels at 500 view angles over 360°.[38] The source focal spot was modeled as a point, while each detector was modeled with an aperture of 1 mm. For each detector pixel and each energy between 20 and 120 keV in 1 keV increments, five rays were forward-projected from the point source and averaged at the detector to reduce aliasing effects. For both detector types, only noise due to photon-counting statistics was modeled.

II.C.3. Material decomposition and reconstruction

Material decomposition into basis functions was performed in sinogram space using maximum likelihood estimation.[12] For each ray, the algorithm finds the coefficients [c_i in Eq. **(3)**] that maximize the likelihood of obtaining the measured data. The decomposition algorithm assumed ideal knowledge of the energy spectrum,

which in practice would be estimated through calibration methods.[39,40] Basis images and energy-integrating images were reconstructed with a filtered backprojection algorithm onto 0.5 mm × 0.5 mm pixels using an apodized ramp filter with 8 cm^{-1} cutoff. Beam hardening correction was not performed for the energy-integrating reconstruction. For all simulations, basis images reconstructed from energy-resolved data encompassing the full FOV (700 detector pixels) were used as a gold standard.

II.C.4. ROI basis decomposition and reconstruction

The truncated and full FOV energy-resolved sinograms were decomposed into three basis functions selected to isolate iodine based on its K-edge: the Klein Nishima equation representing Compton scatter, E^{-3} representing photoelectric effect, and the mass attenuation coefficient of iodine. The projection data from the 300 central detector pixels of the energy-resolved data were extracted to represent a truncated acquisition covering a ∼15 cm diameter ROI. The iodine basis image, which was primarily contained within the ROI, was reconstructed directly from the truncated iodine basis sinogram. An image of the full FOV was reconstructed from the simulated energy-integrating data to serve as a prior image. Reconstruction of the photoelectric and Compton basis images from truncated data was performed using the prior image to estimate energy-resolved data outside the ROI. The reconstruction algorithm proposed in Sec. **II B** and illustrated in Fig. **1** was implemented by first segmenting the prior energy-integrating image based on HU value. To understand the effects of segmentation on the algorithm, the prior image was segmented into three materials (air, water, and bone) and six materials (air, lung, adipose, water, muscle, and bone), using the HU ranges listed in Table **III**.

Table III. HU ranges used to segment the prior energy-integrating image in step 2 of the proposed reconstruction algorithm (Fig. 1).

		Air	**Lung**	**Adipose**	**Water**	**Muscle**	**Bone**
Six materials	HU range	−2000 ⇔ −930	−930 ⇔ −200	−200 ⇔ −5	−5 ⇔ 5	5 ⇔ 280	>280
	Density (g/cm^3)	1.21×10^{-3}	0.30	0.92	1.00	1.16	1.92
Three materials	HU range	−2000 ⇔ −200	N/A	N/A	−200 ⇔ 280	N/A	>280
	Density (g/cm^3)	1.21×10^{-3}	N/A	N/A	1.00	N/A	1.92

Energy-resolved data were estimated for each energy bin of every detector pixel by forward projecting the segmented prior image at 500 view angles using the Siddon ray-tracing algorithm.[38] For each detector pixel, the forward-projector modeled one ray connecting the source to the center of the pixel. For each pixel and energy bin, a monoenergetic forward projection was performed assuming the average energy of the bin, which could be calculated in practice from the spectrum estimated for material decomposition.[39,40] The forward projection also assumed the average attenuation of the segmented materials within the energy bin and an incident number of photons equal to the raw-beam photons detected in the bin, as could be measured by a flat field acquisition. Overall, the prior image was forward-projected with coarser spatial and energy sampling than the original phantom.

The estimated and measured energy-resolved projection data were decomposed into Compton and photoelectric sinograms. Basis sinograms encompassing the full FOV were estimated by merging the 300 central pixels of basis sinograms from measured energy-resolved data with the basis sinograms estimated at the periphery of the detector (i.e., 200 pixels of estimated data on each side of the 300 pixels of measured data). The following method was investigated for blending the measured data inside the ROI with the data estimated outside the ROI. Energy-resolved data were estimated from the prior image and basis decomposition performed

for the 20 edge pixels within and at the boundaries of the truncated data. For each row of each basis sinogram, the ratio of measured to estimated data was calculated and the median ratio value estimated across the 20 pixels inside and at the left edge of the truncated data. The median ratio was also calculated for the 20 pixels inside and at the right edge of the truncated data. The resulting median ratios served as separate weighting factors for the estimated data on the left and right sides of the truncated data for each row in each basis sinogram. To blend the merged sinograms, the 200 pixels of basis sinograms estimated from the energy-integrating data on each side of the truncated data were multiplied by the corresponding weighting factor for each row of each sinogram.

Basis sinograms from full FOV energy-resolved data, truncated energy-resolved data, and truncated energy-resolved data merged and blended with the estimated data (using three- and six-material segmentation), were reconstructed into basis images of the 15 cm × 15 cm central ROI. The absolute error between basis images reconstructed from truncated data and images reconstructed from full FOV data was calculated for the central horizontal row in the ROI. Because the pixel values vary by orders of magnitude between the three basis images, the percent error was calculated for each basis image by normalizing the absolute error by the mean value of a defined structure in each basis image. Figure **3** illustrates the selected structures of interest. For example, the region labeled A in Fig. **3** is located in the heart muscle and is expected to be depicted primarily in the Compton basis image because of its relatively low atomic number. Therefore, the absolute error in the Compton basis image was normalized by the mean Compton basis image value in the heart muscle region (region A). Similarly, the mean values in regions C (calcification) and B (blood pool) normalized the error in the photoelectric and iodine basis images, respectively. The percent error was then plotted for each basis image as a function of distance to the center of the ROI. The noise standard deviation in regions within the ROI was also compared for all methods.

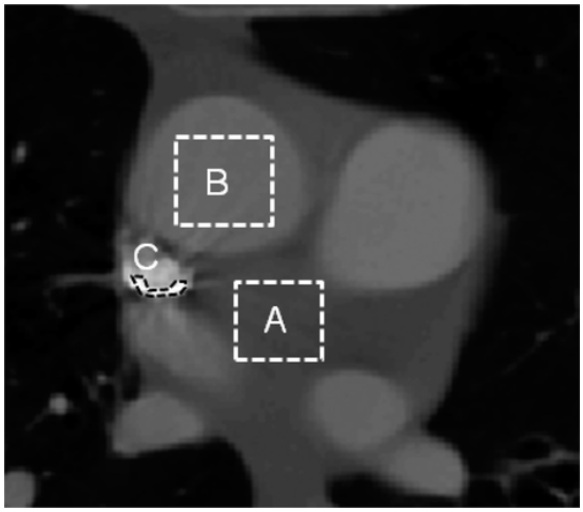

Figure 3. Regions in the heart used to normalize the error between the gold-standard and ROI basis images. The mean value in region A (heart muscle) normalized the Compton basis images, region B (blood pool) normalized iodine basis images, and region C (calcification) normalized photoelectric basis images.

The effects of noise in the prior energy-integrating image on the ROI basis images were examined by simulating a low-dose energy-integrating acquisition with the number of photons reduced by a factor of 200. The reconstructed low-dose energy-integrating image was then segmented into six materials (Table **III**) and forward-projected to estimate energy-bin data outside the ROI. The effect of misalignment between the prior energy-integrating and energy-resolved acquisitions was investigated by translating the energy-integrating image by 1 cm in each of the in-plane directions prior to segmentation into six materials and forward projection.

III. RESULTS

Figure **4** displays the reconstructed energy-integrating image that served as prior information for the proposed reconstruction algorithm. Figure **4** also displays the prior-image segmented into six and three materials using the HU ranges listed in Table **III**. These segmented images were forward-projected to estimate energy-resolved data at the periphery of the ROI.

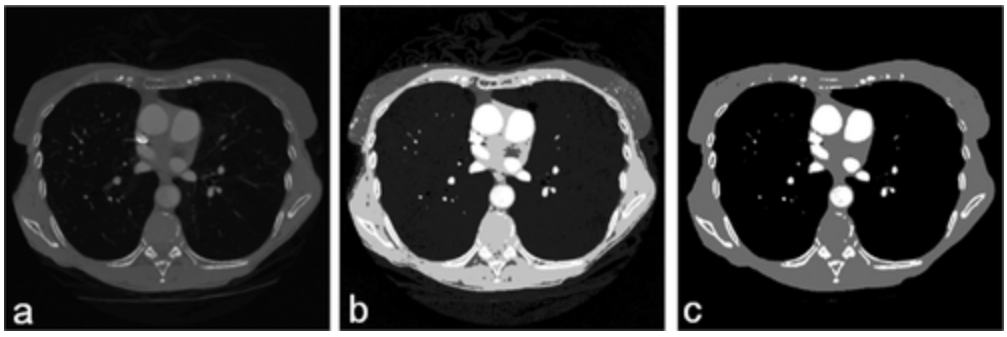

Figure 4. (a) Energy-integrating image used as prior information for estimating energy-resolved data outside the ROI. The prior image was segmented into (b) six materials and (c) three materials using the ranges listed in Table **III**.

Figure **5** compares the central 15 cm × 15 cm ROI of iodine basis images reconstructed from full FOV energy-resolved data and truncated energy-resolved data. The gold-standard basis image of the full FOV is also displayed in order to depict the spatial extent of the basis function. Figure **6** plots the percent error as a function of distance from the center of the ROI for the iodine basis images. As seen in Figs. **5 and 6**, the iodine basis image is primarily contained within the ROI, resulting in negligible truncation artifacts. The error in the truncated iodine basis image (Fig. **6**) was less than 1% for the central 7 cm of the 7.5-cm-radius ROI and 3% at the edge of the ROI.

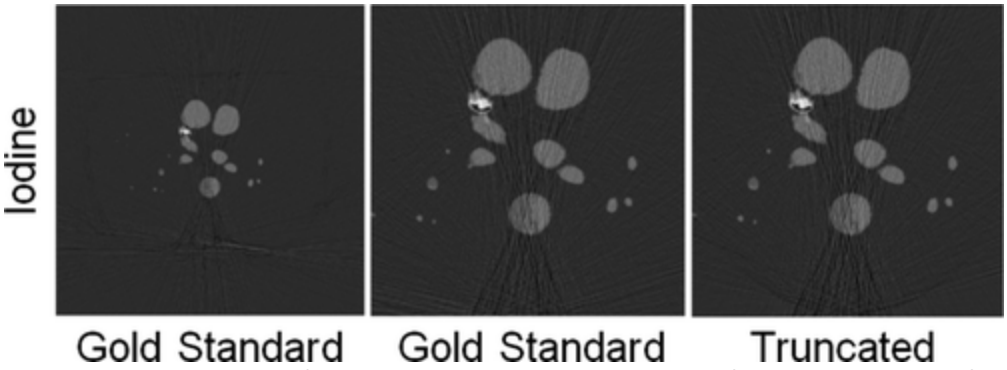

Figure 5. A comparison of iodine basis images reconstructed from gold-standard full FOV energy-resolved data (700 detector pixels) and truncated data (300 detector pixels). All images were reconstructed by filtered backprojection. The first column displays the FOV, while the remaining columns display the central 15 cm × 15 cm ROI.

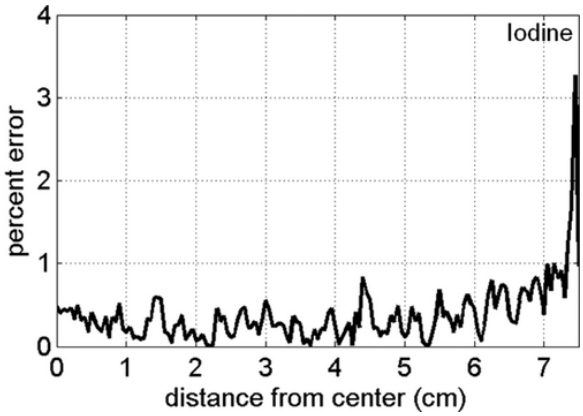

Figure 6 Percent error plotted as a function of distance from the center of the ROI for iodine basis images reconstructed from truncated data.

Figure **7** compares the central 15 cm × 15 cm ROI of Compton and photoelectric basis images reconstructed from full FOV energy-resolved data, truncated energy-resolved data, and truncated energy-resolved data merged and blended with data estimated from the prior energy-integrating image (three-material segmentation). Similar images were obtained using the six-material segmentation. Figures **8 and 9** plot the percent error as a function of distance from the center of the ROI for the Compton and photoelectric basis images, respectively.

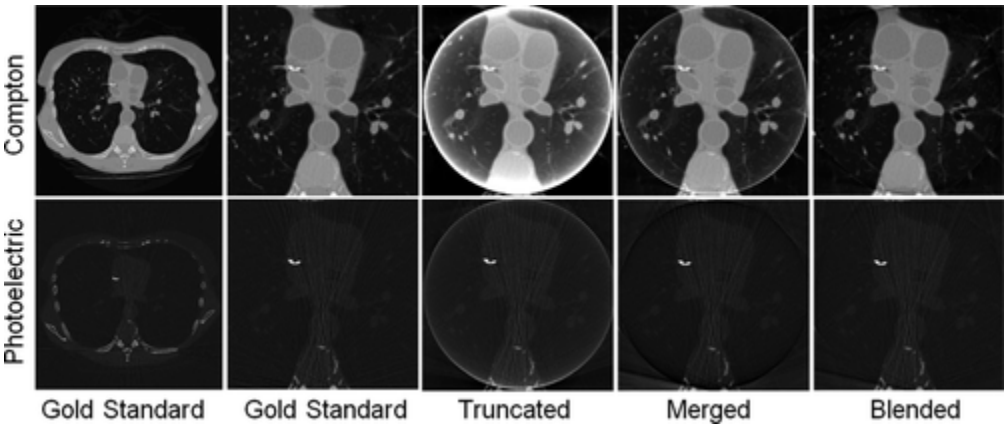

Figure 7. A comparison of Compton and photoelectric basis images reconstructed from gold-standard full FOV energy-resolved data (700 detector pixels), truncated data (300 detector pixels), and truncated data merged with data estimated from the prior energy-integrating data with and without blending (three-material segmentation). The first column displays the FOV, while the remaining columns display the central 15 cm × 15 cm ROI.

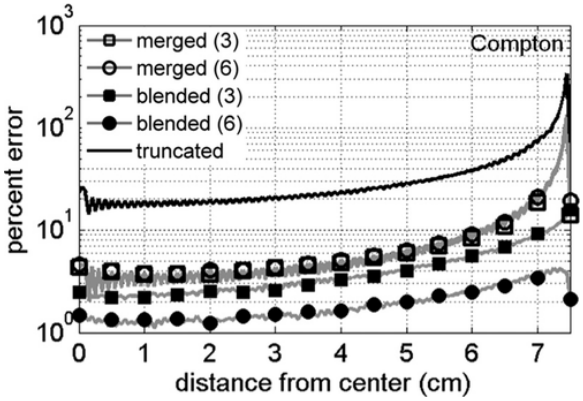

Figure 8. Percent error plotted as a function of distance from the center of the ROI for Compton basis images reconstructed from truncated data and truncated data merged (with and without blending) with data estimated from the prior energy-integrating image segmented into three and six materials.

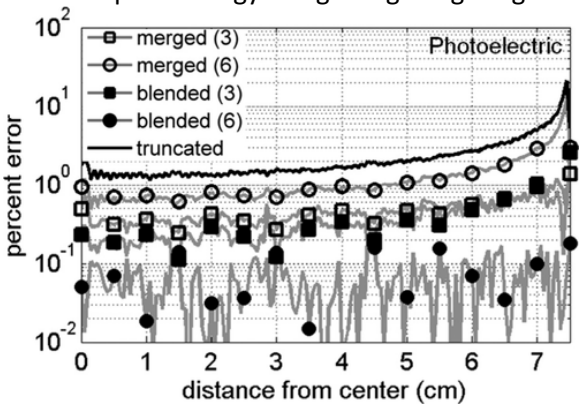

Figure 9. Percent error plotted as a function of distance from the center of the ROI for photoelectric basis images reconstructed from truncated data and truncated data merged (with and without blending) with data estimated from the prior energy-integrating image segmented into three and six materials.

Figure **7** demonstrates that the Compton and photoelectric basis images have contributions throughout the FOV. This causes artifacts in basis images reconstructed from truncated data, including cupping and ringing, with a large artifact at the ROI boundary. Merging the truncated basis sinograms with data estimated outside the ROI reduced the truncation artifacts in the photoelectric and Compton basis images, although cupping, ringing, and boundary artifacts are still visible in Figs. **7–9**. The residual cupping is caused by error in the estimated energy-bin data outside the ROI, while ringing is caused by the sharp discontinuity at the boundary of the ROI. Blending the estimated and measured basis sinograms using the empirically determined weighting factors reduced both the cupping and ringing artifacts. For example, the error in the Compton basis image reconstructed from truncated energy-resolved data ranged from 20% at the center of the ROI to several hundred percent at the edge of the ROI. When the Compton basis sinogram was merged and blended with the data estimated from the prior image (six-material segmentation), the error decreased to 1% at the center, 2% at 5 cm, and 4% at the edge of the ROI. In the photoelectric basis image, truncated data resulted in error ranging from 1% at the center to 20% at the edge. Merging and blending the truncated data with the estimated data reduced the error to less than 1% across the ROI. All decomposition and reconstruction methods successfully separated calcium from iodine. The standard deviation measured in regions labeled A and B in Fig. **3** varied by less than 1% between images reconstructed from gold-standard and merged/blended truncated energy-resolved CT data.

Figure **10** displays the difference between Compton basis images estimated from standard-dose and low-dose prior energy-integrating images. Both basis images were reconstructed after segmenting the energy-integrating image into six materials. The percent error between the blended and gold-standard Compton and photoelectric basis images is also plotted in Fig. **10** for reconstructions using the standard and low-dose energy-integrating prior images. Figure **10** demonstrates noise and differences in mean pixel values outside the ROI, but relatively low error within the ROI. The error plot indicates that the low-dose energy-integrating image reduced the error in the Compton basis image to 1%–3% and had negligible effect on the photoelectric image. The differences in mean pixel value within the ROI occurs because the median HU value of lung tissue in the energy-integrating image was −860 compared to a noise standard deviation of 226 HU for the low-dose image. Because the lower threshold for segmenting lung tissue was −930 (Table **III**), a large number of lung voxels in the noisy prior image were segmented as air, which affected the estimated energy-bin data outside the ROI. For this object, the overall result was a reduction in error, although in other cases the error may increase. The noise standard

deviation in the ROI basis images varied by less than 0.1% for images reconstructed using standard and low-dose prior images.

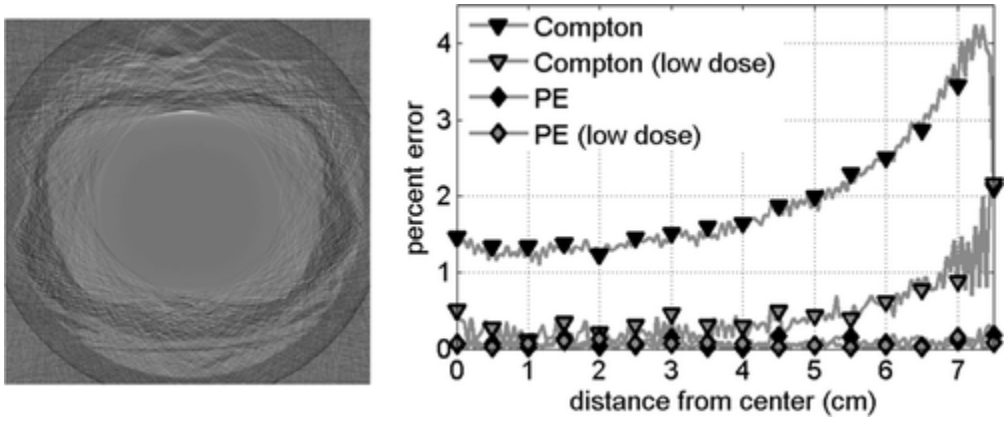

Figure 10. (Left) Difference image between Compton basis images reconstructed using standard and low-dose prior energy-integrating images. (Right) Percent error plotted as a function of distance from the center of the ROI for Compton and photoelectric basis images reconstructed with data estimated from the standard and low-dose prior energy-integrating images.

Figure **11** displays the difference image between the Compton basis images reconstructed using estimates from aligned and misaligned prior energy-integrating images along with a plot of percent error within the ROI. The results demonstrate a negligible effect of the 1 cm misalignment on the ROI basis images.

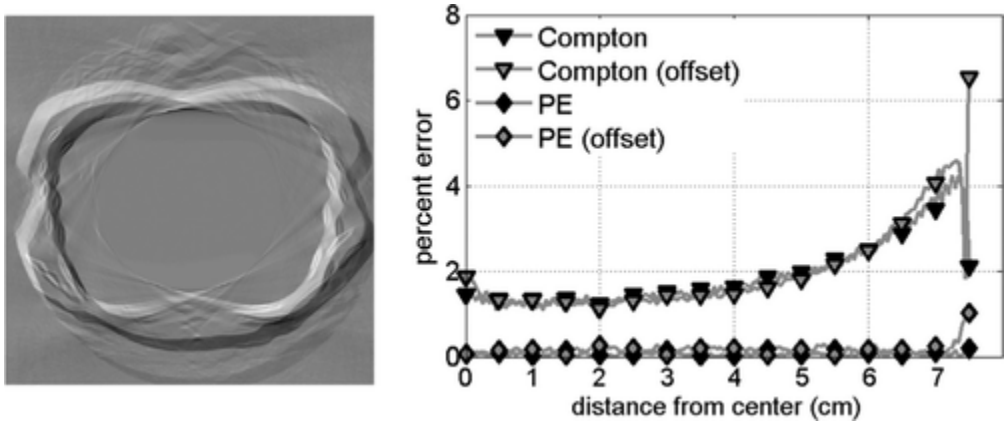

Figure 11. (Left) Difference image between Compton basis images reconstructed using aligned and misaligned prior energy-integrating images. (Right) Percent error plotted as a function of distance from the center of the ROI for Compton and photoelectric basis images reconstructed with data estimated from aligned and misaligned prior energy-integrating images.

IV. DISCUSSION AND CONCLUSIONS

This paper investigated material decomposition and basis image reconstruction for a limited ROI from truncated energy-resolved CT data. Feasibility was demonstrated for quantifying the local density (i.e., concentration) of iodinated contrast material in the heart with 1% error using truncated energy-resolved data and filtered backprojection without prior information. ROI reconstruction from truncated data is possible because material decomposition is performed in sinogram space, with each ray decomposed independently. In addition to cardiac studies with blood-pool contrast agents, this method may be appropriate for quantifying the uptake of targeted K-edge contrast agents.

In the second proposed method, a prior energy-integrating image estimated energy-resolved data outside the ROI in order to reconstruct basis images, which may extend across the FOV. The results demonstrated that when the truncated basis sinograms were merged and blended with basis sinograms estimated outside the ROI, the reconstructed error was less than 1% for the photoelectric basis images and ranged from 1% to 4% for the Compton basis image. The results indicate a factor of 2 reduction in error when the prior image is segmented into six materials compared to three materials.

This paper used the prior energy-integrating image to estimate Compton and photoelectric basis images for an object with K-edge contrast agent primarily localized within the ROI. The algorithm could be similarly applied to noncontrast scans, for example, when characterizing kidney stone composition. Reconstructing K-edge material basis images when the contrast agent is present outside the ROI would be challenging with this algorithm because segmentation of the contrast-agent based on HU value may not be feasible.

This study investigated several sources of error in the acquisition, segmentation, and forward projection of the prior energy-integrating image. The 1%–4% error in basis image value presented in our results was obtained by forward projecting the prior image with a coarse spectrum model consisting of the average energy in each bin, which is expected to be fairly robust to variations in the spectrum. The energy-integrating data were not corrected for beam hardening; therefore, the results include segmentation errors due to beam hardening artifacts. Noise in the energy-integrating image did not affect noise in the ROI basis images but did cause changes in the mean reconstructed values due to the nonlinear thresholding and segmentation step. However, even with an energy-integrating image acquired at 1/200th of the photon fluence of the energy-resolved acquisition, these effects produced errors on the order of 1%–3%. Overall, the noise study suggests that the prior energy-integrating can be acquired at low-dose with minimal impact to the reconstructed ROI basis images. The results also demonstrated negligible impact of a 1 cm misalignment between the energy-integrating and energy-resolved acquisition. In practice, some registration will likely be performed, and these results suggest that the accuracy requirements of this registration may be low. In summary, these results indicate that the reconstructed ROI basis images were accurate to within a few percent, including cases that modeled errors in the prior energy-integrating image.

This study assumed an ideal energy-resolved detector. In practice, energy-resolved detectors may be susceptible to nonidealities including limited energy resolution, spectrum tailing, and errors in the detector thresholds.[11,16,41] Pulse-pileup effects may occur despite the truncated acquisition. These detector nonidealities will impact material decomposition accuracy equally for complete and truncated data, as the decomposition is performed independently for each ray. Detector nonidealities may increase the difference between measured energy-resolved data and data estimated from the prior energy-integrating image, which may introduce errors in the reconstructed ROI basis images. The accuracy of ROI material decomposition in the presence of realistic detector effects requires further study including demonstration of experimental feasibility.

In practice, the prior energy-integrating image could be acquired concurrently with the truncated energy-resolved data, for example, by using a dual-source scanner or a system with a conventional detector combined with a smaller energy-resolved detector offset in the slice direction. Alternatively, the two scans could be acquired at different times. For example, the ROI energy-resolved CT scan could be performed following a diagnostic conventional CT scan. These potential acquisition methods are susceptible to misalignment of the energy-integrating and energy-resolved data due to patient motion and positioning and would likely require registration. The truncated region for avoiding pulse-pileup effects could potentially be identified through scout projections, although feasibility of this method requires further study. The two cases simulated in this study assumed a central ROI, as would be appropriate for cardiac imaging. The physical implementation would be more challenging for an offset ROI. One approach is to reposition the patient to center the ROI. A second

approach is to move a collimator and potentially the detector in a sinusoidal translational pattern during gantry rotation.

In summary, this work investigated reconstructing basis images in a limited ROI from truncated energy-resolved CT data. The study demonstrated that the density of localized K-edge contrast agents can be estimated to within 1% error using filtered backprojection without prior information. Images of general basis functions in the case of localized-contrast or noncontrast scans can be reconstructed with 1% error at the center of the ROI and 1%–4% error at the edge of the ROI using a prior energy-integrating image. Acquiring energy-resolved data for a limited ROI may avoid the count-rate limitations of available photon-counting detectors.

REFERENCES

1 T. Johnson *et al*., " Material differentiation by dual energy CT: Initial experience," *Eur. Radiol.* **17**(6), 1510– 1517 (2007).10.1007/s00330-006-0517-6

2 A. Primak, J. Fletcher, T. Vrtiska, O. Dzyubak, J. Lieske, M. Jackson, J. Williams, Jr., and C. McCollough, " Noninvasive differentiation of uric acid versus non-uric acid kidney stones using dual-energy CT," *Acad. Radiol.* **14**(12), 1441– 1447 (2007).10.1016/j.acra.2007.09.016

3 A. Graser, T. Johnson, M. Bader, M. Staehler, N. Haseke, K. Nikolaou, M. Reiser, C. Stief, and C. Becker, " Dual energy CT characterization of urinary calculi: Initial in vitro and clinical experience," *Invest. Radiol.* **43**(2), 112– 119 (2008).10.1097/RLI.0b013e318157a144

4 A. Graser, T. Johnson, H. Chandarana, and M. Macari, " Dual energy CT: Preliminary observations and potential clinical applications in the abdomen," *Eur. Radiol.* **19**(1), 13– 23 (2009).10.1007/s00330-008-1122-7

5 B. Ruzsics, H. Lee, P. Zwerner, M. Gebregziabher, P. Costello, and U. Schoepf, " Dual-energy CT of the heart for diagnosing coronary artery stenosis and myocardial ischemia-initial experience," *Eur. Radiol.* **18**(11), 2414– 2424 (2008).10.1007/s00330-008-1022-x

6 J. Fletcher, N. Takahashi, R. Hartman, L. Guimaraes, J. Huprich, D. Hough, L. Yu, and C. McCollough, " Dual-energy and dual-source CT: Is there a role in the abdomen and pelvis?," *Radiol. Clin. North Am.* **47**(1), 41– 57 (2009).10.1016/j.rcl.2008.10.003

7 R. E. Alvarez and A. Macovski, " Energy-selective reconstructions in x-ray computerised tomography," *Phys. Med. Biol.* **21**(5), 733– 744 (1976).10.1088/0031-9155/21/5/002

8 M. Overdick, C. Baumer, K. Engel, J. Fink, C. Herrmann, H. Kruger, M. Simon, R. Steadman, and G. Zeitler, " *Towards direct conversion detectors for medical imaging with x-rays*," in Proceedings of the IEEE Nuclear Science Symposium and Medical Imaging, Dresden, Germany, (2008), pp. 1527– 1535.

9 F. Kelcz, P. Joseph, and S. Hilal, " Noise considerations in dual energy CT scanning," *Med. Phys.* **6**, 418 (1979).10.1118/1.594520

10 R. Alvarez, J. Seibert, and S. Thompson, " Comparison of dual energy detector system performance," *Med. Phys.* **31**, 556– 565 (2004).10.1118/1.1645679

11 J. P. Schlomka, E. Roessl, R. Dorscheid, S. Dill, G. Martens, T. Istel, C. Bäumer, C. Herrmann, R. Steadman, G. Zeitler, A. Livne, and R. Proksa, " Experimental feasibility of multi-energy photon-counting K-edge imaging in pre-clinical computed tomography," *Phys. Med. Biol.* **53**(15), 4031– 4047 (2008).10.1088/0031-9155/53/15/002

12 E. Roessl and R. Proksa, " K-edge imaging in x-ray computed tomography using multi-bin photon counting detectors," *Phys. Med. Biol.* **52**(15), 4679– 4696 (2007).10.1088/0031-9155/52/15/020

13 D. Cormode *et al*., " Atherosclerotic plaque composition: Analysis with multicolor CT and targeted gold nanoparticles," *Radiology* **256**(3), 774– 782 (2010).10.1148/radiol.10092473

14 J. Bulte, " Science to practice: Can CT be performed for multicolor molecular imaging?," *Radiology* **256**(3), 675– 676 (2010).10.1148/radiol.101127

15 L. Wielopolski and R. Gardner, " Prediction of the pulse-height spectral distortion caused by the peak pile-up effect," *Nucl. Instrum. Methods* **133**(2), 303– 309 (1976).10.1016/0029-554X(76)90623-6

16 K. Taguchi, E. Frey, X. Wang, J. Iwanczyk, and W. Barber, " An analytical model of the effects of pulse pileup on the energy spectrum recorded by energy resolved photon counting x-ray detectors," *Med. Phys.* **37**, 3957– 3970 (2010).10.1118/1.3429056
17 E. Roessl, J. Schlomka, and R. Proksa, " *Edge-on semiconductor x-ray detectors-towards high-rate counting computed tomography*," in Proceedings of the IEEE Nuclear Science Symposium and Medical Imaging, Dresden, Germany, (2008), pp. 1748– 1751.
18 M. Overdick, C. Baumer, K. Engel, J. Fink, C. Herrmann, H. Kruger, M. Simon, R. Steadman, and G. Zeitler, " Status of direct conversion detectors for medical imaging with x-rays," *Nucl. Sci., IEEE Trans.* **56**(4), 1800– 1809 (2009).10.1109/TNS.2009.2025041
19 P. Johns and M. Yaffe, " X-ray characterisation of normal and neoplastic breast tissues," *Phys. Med. Biol.* **32**(6), 675– 695 (1987).10.1088/0031-9155/32/6/002
20 N. Barradas and M. Reis, " Accurate calculation of pileup effects in PIXE spectra from first principles," *X-Ray Spectrom.* **35**(4), 232– 237 (2006).10.1002/xrs.v35:4
21 K. Taguchi, S. Srivastava, H. Kudo, and W. Barber, " *Enabling photon counting clinical x-ray CT*," in Proceedings of the IEEE Nuclear Science Symposium and Medical Imaging Conference, Orlando, FL, (2009), pp. 3581– 3585.
22 Y. Zou and X. Pan, " Exact image reconstruction on PI-lines from minimum data in helical cone-beam CT," *Phys. Med. Biol.* **49**, 941 (2004).10.1088/0031-9155/49/6/006
23 F. Noo, R. Clackdoyle, and J. Pack, " A two-step Hilbert transform method for 2D image reconstruction," *Phys. Med. Biol.* **49**, 3903 (2004).10.1088/0031-9155/49/17/006
24 S. Cho, J. Bian, C. Pelizzari, C. Chen, T. He, and X. Pan, " Region-of-interest image reconstruction in circular cone-beam microCT," *Med. Phys.* **34**, 4923– 4933 (2007).10.1118/1.2804924
25 H. Kudo, M. Courdurier, F. Noo, and M. Defrise, " Tiny a priori knowledge solves the interior problem in computed tomography," *Phys. Med. Biol.* **53**, 2207 (2008).10.1088/0031-9155/53/9/001
26 K. Taguchi, J. Xu, S. Srivastava, B. M. W. Tsui, J. Cammin, and Q. Tang, " Interior region-of-interest reconstruction using a small, nearly piecewise constant subregion," *Med. Phys.* **38**, 1307– 1312 (2011).10.1118/1.3549763
27 L. Chen *et al*., " Dual resolution cone beam breast CT: A feasibility study," *Med. Phys.* **36**, 4007– 4014 (2009).10.1118/1.3187225
28 L. Chen, C. Shaw, M. Altunbas, C. Lai, X. Liu, T. Han, T. Wang, W. Yang, and G. Whitman, " Feasibility of volume-of-interest (VOI) scanning technique in cone beam breast CTA preliminary study," *Med. Phys.* **35**, 3482 (2008).10.1118/1.2948397
29 R. Chityala, K. Hoffmann, S. Rudin, and D. Bednarek, " Region of interest (ROI) computed tomography (CT): Comparison with full field of view (FFOV) and truncated CT for a human head phantom," *Proc.-SPIE* **5745**(1), 583– 590 (2005).10.1117/12.595430
30 S. Schafer, P. Noël, A. Walczak, and K. Hoffmann, " Filtered region of interest cone-beam rotational angiography," *Med. Phys.* **37**, 694– 703 (2010).10.1118/1.3284540
31 C. Lai *et al*., " Reduction in x-ray scatter and radiation dose for volume-of-interest (VOI) cone-beam breast CTA phantom study," *Phys. Med. Biol.* **54**, 6691– 6709 (2009).10.1088/0031-9155/54/21/016
32 M. Petersilka, H. Bruder, B. Krauss, K. Stierstorfer, and T. Flohr, " Technical principles of dual source CT," *Eur. J. Radiol.* **68**(3), 362– 368 (2008).10.1016/j.ejrad.2008.08.013
33 P. Engler and W. Friedman, " Review of dual-energy computed tomography techniques," *Mater. Eval.* **48**, 623– 629 (1990).
34 J. DeMarco, T. Solberg, and J. Smathers, " A CT-based Monte Carlo simulation tool for dosimetry planning and analysis," *Med. Phys.* **25**, 1– 11 (1998).10.1118/1.598167
35 M. Berger, J. Hubbell, S. Seltzer, J. Chang, J. Coursey, R. Sukumar, and D. Zucker, " XCOM: Photon cross sections database," *NIST Standard Reference Database* **8**, 87– 3597 (1998).
36 ICRU, " Tissue substitutes in radiation dosimetry and measurement," Technical Report No. 44 (International Commission on Radiation Units and Measurements, Inc., Bethesda, MA, 1989).

37 K. Cranley, B. Gilmore, G. Fogarty, and L. Desponds, “IPEM Report 78: Catalogue of diagnostic x-ray spectra and other data,” Technical Report No. 78 (The Institute of Physics and Engineering in Medicine (IPEM), 1997).
38 R. Siddon, “ Fast calculation of the exact radiological path for a three-dimensional CT array,” *Med. Phys.* **12**, 252– 256 (1985).10.1118/1.595715
39 E. Sidky, L. Yu, X. Pan, Y. Zou, and M. Vannier, “ A robust method of x-ray source spectrum estimation from transmission measurements: Demonstrated on computer simulated, scatter-free transmission data,” *J. Appl. Phys.* **97**, 124701 (2005).10.1063/1.1928312
40 X. Duan, J. Wang, L. Yu, S. Leng, and C. McCollough, “ CT scanner x-ray spectrum estimation from transmission measurements,” *Med. Phys.* **38**(2), 993– 997 (2011).10.1118/1.3547718
41 X. Wang, D. Meier, S. Mikkelsen, G. Maehlum, D. Wagenaar, B. Tsui, B. Patt, and E. Frey, “ MicroCT with energy-resolved photon-counting detectors,” *Phys. Med. Biol.* **56**, 2791 (2011).10.1088/0031-9155/56/9/011